

Chromo-Rayleigh Interactions of Dark Matter

Yang Bai and James Osborne

Department of Physics, University of Wisconsin-Madison, Madison, WI 53706, USA

Abstract

For a wide range of models, dark matter can interact with QCD gluons via chromo-Rayleigh interactions. We point out that the Large Hadron Collider (LHC), as a gluon machine, provides a superb probe of such interactions. In this paper, we introduce simplified models to UV-complete two effective dark matter chromo-Rayleigh interactions and identify the corresponding collider signatures, including four jets or a pair of di-jet resonances plus missing transverse energy. After performing collider studies for both the 8 TeV and 14 TeV LHC, we find that the LHC can be more sensitive to dark matter chromo-Rayleigh interactions than direct detection experiments and thus provides the best opportunity for future discovery of this class of models.

1 Introduction

Although there is no doubt that dark matter interacts gravitationally both among itself and with the Standard Model (SM) particles, we still have no convincing evidence for other dark matter interactions. Among the three forces in the SM, dark matter can not have order-one couplings under the electroweak forces. Otherwise, it will either emit photons or scatter off nuclei with a too-large cross section in direct detection experiments. Suppressed couplings to the Z boson or the Higgs boson will be probed further in upcoming dark matter experiments [1]. For QCD interactions, the dark matter particle can not have a color charge due to confinement. If, instead, it is a QCD composite particle, the hadronic bound states should have a large interaction strength with SM pions and thus have a large scattering cross section with nucleons. This type of dark matter can not penetrate the Earth to reach detectors in underground direct detection experiments, but satellite-based X-ray quantum calorimetry experiments impose stringent bounds on this scenario [2].

Another way for dark matter to interact with gluons is through effective contact interactions, comparable to photon–molecule Rayleigh interactions. Introducing such higher-dimensional effective operators to describe dark matter *chromo-Rayleigh* interactions is then independent of whether the dark matter is elementary or composite. For instance, in supersymmetric models the neutralino can couple to two gluons via a stop–top quark loop. In extra-dimensional models, a similar loop from the top quark and its Kaluza-Klein mode can generate the effective chromo-Rayleigh dark matter interaction [3]. Composite dark matter models can also generate chromo-Rayleigh interactions, with strengths typically suppressed by the composite scale [4]. In this paper, we perform a generic study on dark matter chromo-Rayleigh interactions. We pay particular attention to collider searches and the potential signatures associated with chromo-Rayleigh interactions. This study is similar to searches for electrical Rayleigh interactions of dark matter in Ref. [5,6], where the electrically charged particles can be searched for directly at the LHC.

For simplicity, we choose the dark matter particle to be a complex scalar denoted as X . We study two types of dimension-six interactions: $X^\dagger X G^2$ and $(XX - X^\dagger X^\dagger) G\tilde{G}$, where G is the QCD field tensor. For direct detection searches, the first operator provides spin-independent scattering while the second operator provides spin-dependent and momentum-suppressed scattering. For collider searches, the standard model independent signature is a mono-jet plus missing transverse energy. Taking into account the well-known limitations of such searches [7–24], we introduce simplified models to UV-complete these two operators. Collider signatures owing to such UV-completions depend strongly on how the colored mediators decay. We discuss several possible signatures, including multi-jets and

pair-produced di-jet resonances with missing transverse energy.

The rest of this paper is organized as follows. In Section 2, we work out the dark matter thermal relic abundance, direct detection cross sections, and collider constraints from the effective chromo-Rayleigh contact interactions. In Section 3, we introduce two simplified models to UV-complete the previous contact operators. Section 3.1 introduces a scalar color-octet with the signature of four jets plus missing transverse energy, Sections 3.2–3.3 introduce two fermion color-triplets with the additional signature of paired di-jet resonances plus missing transverse energy, and Section 4 offers a comparison to direct detection experiments. We conclude in Section 5.

2 Contact Interactions

Our model consists of a complex scalar dark matter field, X , which is a singlet under the SM gauge group. We introduce the following two CP -conserving, dimension six operators coupling dark matter to the gluon field

$$\mathcal{O}_1^{\text{cRayleigh}} = \frac{\alpha_s}{4\pi\Lambda_1^2} X^\dagger X G_{\mu\nu}^a G^{a\mu\nu}, \quad (1)$$

$$\mathcal{O}_2^{\text{cRayleigh}} = \frac{i\alpha_s}{4\pi\Lambda_2^2} (XX - X^\dagger X^\dagger) G_{\mu\nu}^a \tilde{G}^{a\mu\nu}, \quad (2)$$

where Λ_i is the cutoff scale and $\tilde{G}^{a\mu\nu} = \frac{1}{2}\epsilon^{\mu\nu\alpha\beta}G_{\alpha\beta}^a$ is the dual gluon field strength tensor. The overall operator normalization accounts for a loop factor. In order for X to be stable, we impose a \mathbb{Z}_2 symmetry under which X is odd. Based on these two effective operators, we first calculate the thermal relic abundance, direct detection cross sections, and collider constraints.

2.1 Thermal Relic Abundance

Depending on the UV physics, the dark matter sector could be more complicated than just one state. Therefore, the dark matter thermal relic abundance calculation based entirely on the operators in Eqs. (1) and (2) can only provide a guidance for the potential parameter space in M_X and Λ_i for thermal dark matter. For the first operator, we have the dark matter self-annihilation rate from the process $X^\dagger X \rightarrow GG$ as

$$\frac{1}{2} \left[\langle \sigma v \rangle (X^\dagger X \rightarrow GG) \right] = \frac{1}{2} \left[\frac{\alpha_s^2}{\pi^3} \frac{M_X^2}{\Lambda_1^4} \right] \equiv s, \quad (3)$$

to leading order in the dark matter's relative velocity v expansion. Here, the overall factor of $1/2$ is due to the relic density being comprised of particles and antiparticles. For the second operator,

we have the annihilation rate from the process $XX[X^\dagger X^\dagger] \rightarrow GG$, in terms of components with $X = (X_R + iX_I)/\sqrt{2}$, as

$$\frac{1}{2} [\langle \sigma v \rangle (X_R X_I \rightarrow GG)] = \frac{1}{2} \left[\frac{\alpha_s^2}{\pi^3} \frac{M_X^2}{\Lambda_2^4} \right] \equiv s. \quad (4)$$

The dark matter relic abundance is inversely proportional to the annihilation rate and has a formula $\Omega_X h^2 \approx 1.07 \times 10^9 \text{ GeV}^{-1} x_F / (\sqrt{g^*} M_{\text{pl}} s)$ with g^* as the number of relativistic degrees of freedom at the freeze-out temperature and is taken to be 86.25 and the Planck scale is $M_{\text{pl}} = 1.22 \times 10^{19} \text{ GeV}$. The freeze-out temperature x_F is given by $x_F = \ln [0.05 g M_{\text{pl}} M_X s / (\sqrt{g^*} x_F)]$ with $g = 2$ and is typically $\mathcal{O}(20)$.

2.2 Direct Detection

For the first operator $\mathcal{O}_1^{\text{cRayleigh}}$, we can use the matrix element of $G_{\mu\nu}^a G^{a\mu\nu}$ inside a nucleon to derive the dark matter coupling to two nucleons. The trace anomaly of the QCD energy-momentum tensor implies [25, 26]

$$m_N \langle N|N \rangle = \langle N| \sum_{1 \leq i \leq n_f} m_i \bar{\psi}_i \psi_i (1 + \gamma) + \left(\frac{\beta^{n_f}}{2\alpha_s^2} \right) \alpha_s G_{\mu\nu}^a G^{a\mu\nu} |N \rangle, \quad (5)$$

where $\beta^{n_f} = -(11 - 2n_f/3)\alpha_s^2/4\pi$ is the beta function at leading order, n_f is the number of quarks, and γ is the anomalous dimension of the quark field. So, at leading order in α_s and keeping only $n_f = 3$ light quarks, we have

$$\langle N| \alpha_s G_{\mu\nu}^a G^{a\mu\nu} |N \rangle = \frac{8\pi}{9} m_N \left[\frac{1}{m_N} \langle N| m_u \bar{u}u + m_d \bar{d}d + m_s \bar{s}s |N \rangle - 1 \right] \equiv \frac{8\pi}{9} m_N [(f_u + f_d + f_s) - 1]. \quad (6)$$

Recent Lattice QCD updates of the calculation for the strange quark matrix element has $f_u + f_d + f_s = 0.085_{-0.014}^{+0.022}$ [27]. In our numerical calculation, we will use $\langle N| \alpha_s G_{\mu\nu}^a G^{a\mu\nu} |N \rangle \approx -2.56 m_N$. The formula of the scattering cross section is then calculated to be

$$\sigma_{XN}^{\text{SI}} = \frac{\kappa^2 m_N^4}{4\pi \Lambda_1^4 (m_N + M_X)^2}, \quad (7)$$

with $\kappa = \frac{2}{9}(f_u + f_d + f_s - 1) \approx -0.20$.

For the second operator, $\mathcal{O}_2^{\text{cRayleigh}}$, we need to know the matrix element of $G\tilde{G}$ inside a nucleon. This matrix element is related to the anomalous divergence of the iso-singlet axial current operator by

$$\sum_{i=1, \dots, n_f} \partial^\mu (\bar{\psi}_i \gamma_\mu \gamma_5 \psi_i) = \frac{n_f}{4\pi} \alpha_s G_{\mu\nu}^a \tilde{G}^{a\mu\nu} + \sum_{i=1, \dots, n_f} 2i m_i \bar{\psi}_i \gamma_5 \psi_i. \quad (8)$$

In the large- N_c and chiral limit and using the relation $\langle N | \bar{u}i\gamma_5 u + \bar{d}i\gamma_5 d + \bar{s}i\gamma_5 s | N \rangle = 0$, one finds [28–30]

$$\langle p | \frac{\alpha_s}{8\pi} G_{\mu\nu}^a \tilde{G}^{a\mu\nu} | p \rangle = 389 \text{ MeV} \equiv \eta_p m_p, \quad \langle n | \frac{\alpha_s}{8\pi} G_{\mu\nu}^a \tilde{G}^{a\mu\nu} | n \rangle = -2 \text{ MeV} \equiv \eta_n m_n, \quad (9)$$

where the dimensionless parameters are $\eta_p \approx 0.41$ and $\eta_n \approx -0.0021$ (the instanton calculation in Ref. [31] obtained dramatically different numbers). The large difference between η_p and η_n indicates a large isospin violation for pseudo-scalar coupling to nucleons. One can then use the matrix elements to translate \mathcal{O}_2 to the interaction between dark matter and nucleons, giving

$$\frac{2i\eta_N m_N}{\Lambda_2^2} (X X - X^\dagger X^\dagger) \bar{N} i\gamma_5 N. \quad (10)$$

In the non-relativistic limit, one has $\bar{N} i\gamma_5 N \approx 2i\vec{q} \cdot \vec{s}$ with \vec{q} as the exchange momentum of the scattering process and \vec{s} as the spin of a nucleon. So, for this interaction, we have both spin-dependent and momentum-suppressed scattering. The spin-dependent differential scattering cross section is

$$\frac{d\sigma_{XN}^{\text{SD}}}{d\cos\theta} = \frac{\eta_N^2 m_N^2}{2\pi\Lambda_2^4} \frac{q^2}{(m_N + M_X)^2}. \quad (11)$$

For $M_X \sim 100$ GeV, a small cutoff scale of $\Lambda_2 \sim 100$ GeV, and a typical exchange momentum of $q \sim \mu_{XA} v \sim 100$ MeV, the spin-dependent scattering cross section of dark matter off a proton is 10^{-7} pb. This is far below the current direct detection experimental bound [32, 33].

2.3 Collider Constraints

For the two operators considered here, the universal signature at the LHC is that of a mono-jet plus missing transverse energy [34, 35]. For fermion dark matter coupling to two gluons, both the CMS [36] and ATLAS [37] collaborations have imposed limits on the cutoffs of the effective operators. To estimate the constraints on our scalar dark matter case, we use `FeynRules` [38] to generate a model file for `MadGraph` [39]. We then use `Pythia` [40] to shower and hadronize the parton-level events. Finally, we use `PGS` [41] to cluster hadrons into jets and simulate detector effects.

Following the same analysis procedure from the CMS collaboration in Ref. [36] at 8 TeV and with 19.7 fb^{-1} luminosity, we have found that imposing a cut on the missing transverse energy $E_T^{\text{miss}} > 500$ GeV (or requiring less than 164 signal events) provides the strongest bounds for a wide range of dark matter masses. We show the constraints on the cutoffs of the effective operators in Table 1 for different dark matter masses. The constraints stay constant for light dark matter below 100 GeV and become weaker as one increases the dark matter mass beyond around 100 GeV. One can also see that for heavier dark matter beyond 200 GeV, the constraints become much weaker such that the cutoff is even below M_X , which indicates a breakdown of the perturbative description of the effective field theory.

M_X (GeV)	Λ_1 (GeV)	Λ_2 (GeV)
1	130	170
10	120	180
100	120	180
200	110	160
400	90	130

Table 1: The collider constraints on the cutoff of the effective operators for different dark matter masses at 90% CL. The mono-jet analysis with $E_T^{\text{miss}} > 500$ GeV from the CMS collaboration in Ref. [36] has been used.

3 Simplified UV-completion Models

As already can be seen from Table 1, the constraints on the cutoffs of the contact operators from the mono-jet searches are not that stringent. For a 100 GeV dark matter particle, the constrained cutoff is just comparable to the dark matter mass. This calls for UV-completed models to reduce the uncertainties from an effective field theory description. In this section, we consider several classes of models to illustrate that collider signatures beyond the mono-jet may provide a more sensitive probe of dark matter chromo-Rayleigh interactions.

One of the simplest ways to UV-complete the two operators in Eqs. (1)(2) is to introduce a color-neutral scalar or pseudo-scalar, which can couple to two gluons either from the top quark or new heavy colored fermion loops. For the operator $\mathcal{O}_1^{\text{cRayleigh}}$, one can simply introduce a Higgs-portal dark matter coupling like $XX^\dagger HH^\dagger$. With the effective coupling of the Higgs boson with two gluons in the SM, one generates the coupling of two dark matter particles to two gluons. For the second operator $\mathcal{O}_2^{\text{cRayleigh}}$, the two-Higgs-doublet-portal dark matter models have a pseudo-scalar as a mediator to generate the dark matter chromo-Rayleigh interactions (see Refs. [19, 20, 42, 43]). The existing search strategy for the Higgs-portal or pseudo-scalar-portal dark matter should cover this class of UV-completion models [44]. Therefore, we do not discuss this case in great detail. Instead, we consider two other ways to UV-complete the two operators and point out more interesting collider signatures.

3.1 QCD-charged Particle Mediation for $\mathcal{O}_1^{\text{cRayleigh}}$

In this subsection, we examine a class of models with additional QCD-charged scalars to generate the effective chromo-Rayleigh interaction of $\mathcal{O}_1^{\text{cRayleigh}}$. For specificity's sake, we introduce a real color-

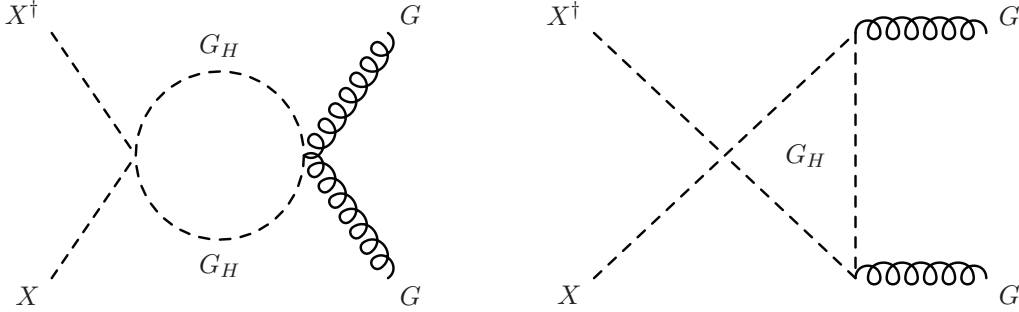


Figure 1: Representative loop diagrams for generating $\mathcal{O}_1^{\text{cRayleigh}}$ via colored scalar loops.

octet and electroweak-singlet scalar,¹ G_H^a with $a = 1, \dots, 8$ and a mass of M_{G_H} , which, for example, appears in the Renormalizable Coloron Model (ReCoM) [45, 46]. At the renormalizable level, one has the following interaction coupling two G_H 's to two dark matter fields

$$\mathcal{L} \supset -\frac{\lambda}{2} G_H^a G_H^a X^\dagger X. \quad (12)$$

At one-loop level, the effective operator can be generated through the diagrams in Fig. 1 and has the following calculated form

$$F(\tau) \frac{\lambda}{8 M_{G_H}^2} \frac{\alpha_s}{4\pi} X^\dagger X G_{\mu\nu}^a G^{a\mu\nu}, \quad (13)$$

where the form factor $F(\tau)$, with $\tau = (p_1 + p_2)^2 / (4M_{G_H}^2)$, is one in the limit $\tau \rightarrow 0$. Here, p_1 and p_2 are the gluon momenta pointing to the vertex. In the limit that $M_{G_H} \gg M_X$ and with small gluon momenta much below $|p_1 + p_2|$, one can match the colored particle mass to the effective operator cutoff defined in Eq. (1) to obtain

$$\Lambda_1^2 = \frac{8}{\lambda} M_{G_H}^2. \quad (14)$$

For this class of UV-complete models, one can also work out the collider constraints. Depending on whether the color-octet is odd or even under the dark matter \mathcal{Z}_2 , one has different decay channels for G_H^a . If it is \mathcal{Z}_2 -even, the following renormalizable G_H cubic self-interaction can make G_H unstable

$$\mu_G d_{abc} G_H^a G_H^b G_H^c, \quad (15)$$

with d_{abc} the totally-symmetric $SU(3)_{\text{QCD}}$ tensor. This introduces the decay of G_H into two gluons at one loop with a width of [45, 47]

$$\Gamma(G_H \rightarrow gg) = \frac{15 \alpha_s^2 \mu_G^2}{128 \pi^3 M_{G_H}} \left(\frac{\pi^2}{9} - 1 \right)^2. \quad (16)$$

¹A similar analysis can be performed for other QCD representations.

\mathcal{Z}_2 -even G_H can be pair-produced at the LHC from their QCD interactions, which then decay into paired dijets. Following the same reinterpretation of the experimental data as in Ref. [48], we find that the current searches for paired dijet resonances at the 8 TeV LHC have set a constraint on its mass of [49]

$$M_{G_H} \gtrsim 520 \text{ GeV}, \quad \text{for } \mathcal{Z}_2\text{-even } G_H, \quad (17)$$

where we have only included the QCD productions.

If G_H is \mathcal{Z}_2 -odd, the dark matter particle X has to appear in the G_H decay products. The operators mediating G_H decaying to X first occur at the dimension six level and contain the following two parity-conserving operators

$$\frac{D_\mu G_H^a \partial_\nu X G^{a\mu\nu}}{\Lambda_1'^2} + h.c., \quad \frac{G_H^a X \tilde{H} \bar{Q}_L t^a t_R}{\Lambda_1''^2} + h.c.. \quad (18)$$

Here, t^a with $a = 1, 2, \dots, 8$ are the $SU(3)_{\text{QCD}}$ generators. For the second operator, we have only included the top quark by assuming that the coupling is proportional to the quark mass. Using the equation of motion, $D_\mu G^{a\mu\nu} = -g_s \bar{q} \gamma^\nu t^a q$, the first decay-inducing operator becomes

$$\frac{g_s}{\Lambda_1'^2} G_H^a \partial_\nu X \bar{q} \gamma^\nu t^a q. \quad (19)$$

As a result, the decay channels of the colored state G_H are mainly $G_H \rightarrow X \bar{q} q$. For each flavor, the three-body decay width is calculated to be

$$\Gamma(G_H \rightarrow X \bar{q} q) = \frac{g_s^2}{3 \cdot 2^9 \pi^3 \Lambda_1'^4} \int_{4m_q^2}^{(M_{G_H} - M_X)^2} ds \left(1 + \frac{2m_q^2}{s}\right) \left(1 - \frac{4m_q^2}{s}\right)^{1/2} \left[\frac{M_X^4 + (M_{G_H}^2 - s)^2 - 2M_X^2(M_{G_H}^2 + s)}{M_{G_H}^2} \right]^{3/2} \quad (20)$$

Choosing $g_s = 1.1$, $M_{G_H} = 500 \text{ GeV}$, $M_X = 10 \text{ GeV}$, $\Lambda_1' = 1 \text{ TeV}$, and neglecting the quark mass, $\Gamma = 0.0002 \text{ GeV}$ for each flavor and G_H can decay promptly for collider studies.

From the above assumptions, the collider signature for pair-produced \mathcal{Z}_2 -odd G_H contains $4j + E_T^{\text{miss}}$, $t\bar{t} + 2j + E_T^{\text{miss}}$ and $2t + 2\bar{t} + E_T^{\text{miss}}$. Generically, the top-quark rich final state can be easily searched for at the LHC. So, we concentrate on the first operator in Eq. (18) and derive a more conservative bound based mainly on the $4j + E_T^{\text{miss}}$ final state. Following the analysis in Ref. [50] at the 8 TeV LHC with 19.5 fb^{-1} , we find that the set of cuts with $300 < \cancel{H}_T < 450 \text{ GeV}$, $800 < H_T < 1000 \text{ GeV}$, $3 \leq N_{\text{jets}} \leq 5$ with $p_T(j) > 50 \text{ GeV}$ and $|\eta| < 2.5$ provide the best constraint. For $M_{G_H} = 600 \text{ GeV}$ and $M_X = 10 \text{ GeV}$, we have $\text{Br}(G_H \rightarrow 2j + X) = 97.5\%$ and $\text{Br}(G_H \rightarrow t\bar{t} + X) = 2.5\%$. The production cross section at the 8 TeV LHC after this set of cuts is approximately $1.9 \text{ fb} \times K$ with

the K -factor as 1.8 [51]. This amounts to a total of 65.4 events at 19.5 fb^{-1} , which is very close to the allowed number of signal events (65.6 from Ref. [50]) at 90% C.L. So, for a large mass splitting between the color-octet state G_H and the dark matter X , the current LHC bound is

$$M_{G_H} \gtrsim 600 \text{ GeV}, \quad \text{for } \mathcal{Z}_2\text{-odd } G_H. \quad (21)$$

Independent on how G_H decays, we have set a constraint on the G_H mass to be above 500-600 GeV. Using the relation in Eq. (14), this constraint translates to a limit on the effective cutoff scale of $\Lambda_1 \gtrsim 1.5 - 1.7 \text{ TeV}$ for $\lambda = 1$, which is far more stringent than the limits in Table 1 set from the mono-jet search. To compare with the limits from direct detection experiments, we show the reinterpreted collider limits using $\Lambda_1 > 1.7 \text{ TeV}$ for the first chromo-Rayleigh interaction in the left panel of Fig. 7. The left panel of Fig. 7 shows a comparison between the limits on the scattering cross section σ_{XN}^{SI} obtained from direct detection, monojet, and $4j + E_T^{\text{miss}}$ searches.

3.2 QCD-charged Particle Mediation for $\mathcal{O}_2^{\text{cRayleigh}}$

To UV-complete the operator $\mathcal{O}_2^{\text{cRayleigh}}$, we introduce the following CP -conserving Lagrangian

$$\mathcal{L} \supset -y_1 (X + X^\dagger) (\bar{\psi}_1 \psi_2 + \bar{\psi}_2 \psi_1) - (X - X^\dagger) (y_2 \bar{\psi}_1 \gamma_5 \psi_2 + y_2 \bar{\psi}_2 \gamma_5 \psi_1). \quad (22)$$

Here, ψ_1 and ψ_2 are chosen to be QCD triplets and their electroweak quantum numbers will be discussed and specified later. To conserve the dark \mathcal{Z}_2 symmetry, one of the fermion triplets must be \mathcal{Z}_2 -odd while the other is \mathcal{Z}_2 -even. Using the freedom of field redefinitions of ψ_1 and ψ_2 , one can keep the first coupling, y_1 , to be a real number while the second coupling, y_2 , may in general be complex. We choose y_2 to be a real number to satisfy CP symmetry. In terms of the components, $X = (X_R + i X_I)/\sqrt{2}$, we have the interactions

$$\mathcal{L} \supset -\sqrt{2} y_1 X_R (\bar{\psi}_1 \psi_2 + \bar{\psi}_2 \psi_1) - \sqrt{2} i X_I (y_2 \bar{\psi}_1 \gamma_5 \psi_2 + y_2 \bar{\psi}_2 \gamma_5 \psi_1). \quad (23)$$

To preserve C and P , one has X_R to be C -even and P -even, and X_I to be C -even and P -odd. In terms of X_R and X_I , we have the effective operator

$$\mathcal{O}_2^{\text{cRayleigh}} = -\frac{\alpha_s}{2\pi\Lambda_2^2} X_R X_I G_{\mu\nu}^a \tilde{G}^{a\mu\nu}, \quad (24)$$

which conserves both C and P .

At one-loop level, one has the box diagrams in Fig. 2 to generate the effective operator $\mathcal{O}_2^{\text{cRayleigh}}$. In the heavy particle limit with $m_{\psi_1}, m_{\psi_2} \gg M_{X_R}, M_{X_I}$, we have the matching condition (see Appendix A for a more detailed calculation)

$$\Lambda_2^2 = \frac{2 m_{\psi_1} m_{\psi_2}}{|y_1 y_2|}. \quad (25)$$

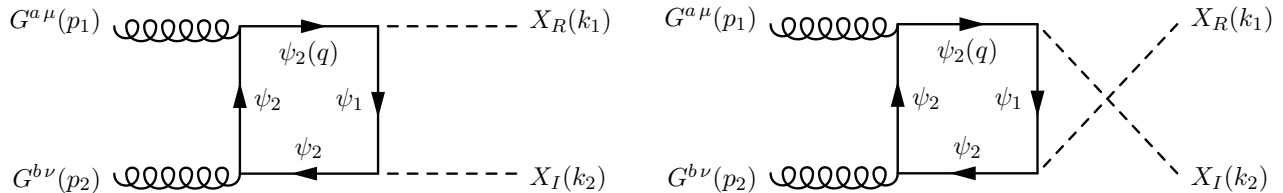


Figure 2: Representative loop diagrams for generating $\mathcal{O}_2^{\text{cRayleigh}}$ via colored fermion loop.

For this specific UV-completion model, the first chromo-Rayleigh interaction can also be generated, since it does not break any discrete symmetries.

If $\text{Im}(y_1 y_2) \neq 0$, the Lagrangian in Eq. (23) is P -conserving but C -breaking, so CP is also broken.² The lowest dimensional effective operator that is C -odd and P -even is at dimension-10, for instance $X_R X_I d_{abc} (D_\mu G_{\alpha\beta}^a) (D_\nu G^{b\nu\alpha}) \tilde{G}^{c\beta\mu}$, further suppressed by powers of the cutoff scale. If parity was broken, lower-dimensional operators like $X_R X_I G_{\mu\nu}^a G^{a\mu\nu}$ could be generated with a stringent bound from the neutron electric dipole moment.

As mentioned before, in order to conserve the dark \mathcal{Z}_2 symmetry the two fields, ψ_1 and ψ_2 , should have opposite dark parity. Fixing the mass relation $m_{\psi_2} > m_{\psi_1}$, we have two cases. The case A has \mathcal{Z}_2 -even ψ_1 and \mathcal{Z}_2 -odd ψ_2 and the case B has \mathcal{Z}_2 -even ψ_2 and \mathcal{Z}_2 -odd ψ_1 . For both cases, we introduce the following dimension-5 operator to mediate the \mathcal{Z}_2 -even particle decaying into two jets,

$$\frac{g_s^2}{4\pi \Lambda_2'} \bar{\psi}_i L \sigma^{\mu\nu} t^a u_R \tilde{G}_a^{\mu\nu}. \quad (26)$$

Here, $i = 1(2)$ for case A(B); the electroweak quantum numbers of ψ_i are then the same as u_R (or d_R). As a result of this decay mode, the unstable particle ψ_i behaves as a dijet resonance at colliders. One could also consider other potential decay channels by introducing the electroweak dipole moment operator, which has a clearer signature at colliders.

For case A with a \mathcal{Z}_2 -even ψ_1 , the collider signature of ψ_1 is pair-produced dijet resonances. The searches at the 8 TeV LHC have set a constraint on its mass [49] as $m_{\psi_1} \gtrsim 500$ GeV. Although the signature is interesting by itself, the discovery of this dijet resonance can not prove that dark matter has been produced at colliders. For the \mathcal{Z}_2 -odd ψ_2 particle, the decay channel is $\psi_2 \rightarrow X + \psi_1 \rightarrow X + 2j$. Depending on the mass splitting of ψ_1 and ψ_2 , one has ψ_1 to be off-shell for $m_{\psi_2} - m_{\psi_1} < M_X$ and on-shell for $m_{\psi_2} - m_{\psi_1} > M_X$. For the off-shell intermediate ψ_1 case, this signature is very similar to the SUSY squark searches with a heavy gluino [50], except with a larger production cross section

²For a complex y_2 with CP -violating interactions, one may wonder about generating the Weinberg operator [52], $f_{abc} G_{\mu\rho}^a G_{\nu\rho}^b \tilde{G}^{c\mu\nu}$. We note that the P conservation forbids the generation of the effective Weinberg operator.

than a single flavor squark. For dark matter mass $M_X \lesssim 100$ GeV, the constraint on the ψ_2 mass is $m_{\psi_2} \gtrsim 850$ GeV, assuming that the signal acceptance is similar to the squark one [50]. For a heavy dark matter mass close to 290 GeV, the constraint becomes weaker and is $m_{\psi_2} \gtrsim 500$ GeV. Using the conversion formula in Eq. (25), we show the constraints from $4j + E_T^{\text{miss}}$ on the effective cutoff for different dark matter masses in the left panel of Fig. 3, by setting $m_{\psi_1} = m_{\psi_2} - M_X$ and $y_1 y_2 = 1$.

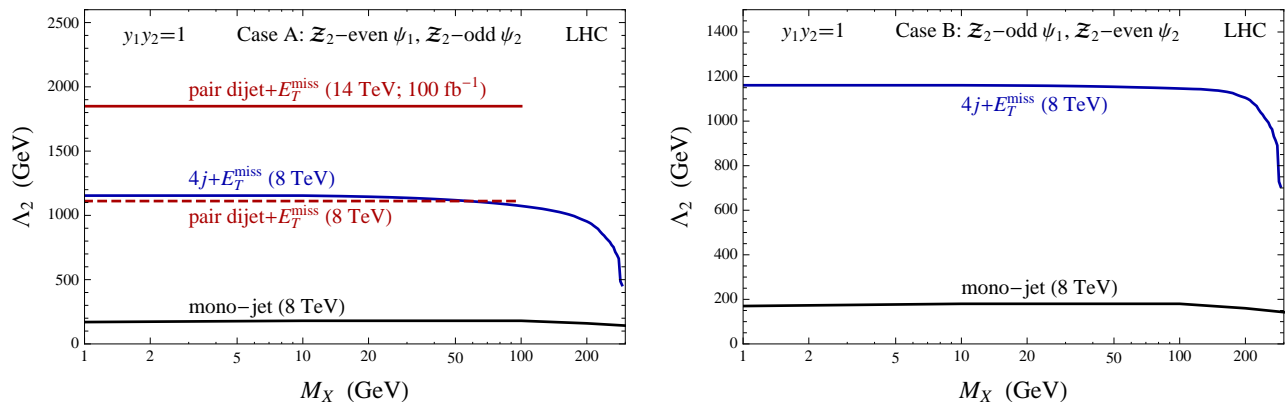


Figure 3: **Left panel:** constraints on the cutoff of the effective operator $\mathcal{O}_2^{\text{cRayleigh}}$ for case A with \mathcal{Z}_2 -even ψ_1 and \mathcal{Z}_2 -odd ψ_2 . **Right panel:** constraints for case B with \mathcal{Z}_2 -odd ψ_1 and \mathcal{Z}_2 -even ψ_2 .

For the on-shell ψ_1 case, the signature is more interesting with a pair of dijet resonances plus a large E_T^{miss} . The relevant production Feynman diagram is shown in the left panel of Fig. 4. We perform a detailed collider study for this interesting signature in Section 3.3. As a comparison, in the left panel of Fig. 3 we show the interpreted constraints for $M_X \lesssim 100$ GeV on the matched cutoff from Eq. (25) for both the 8 TeV LHC with 19.5 fb^{-1} and the 14 TeV LHC with 100 fb^{-1} . One can see a clear improvement on constraining this effective chromo-Rayleigh interaction from a dedicated search beyond the simple mono-jet signature.

For case B with \mathcal{Z}_2 -odd ψ_1 and \mathcal{Z}_2 -even ψ_2 , the searches for pair-produced dijet resonances provide a constraint of $m_{\psi_2} \gtrsim 500$ GeV. The decay of ψ_1 needs to go through an off-shell ψ_2 via $\psi_1 \rightarrow X + \psi_2^* \rightarrow X + 2j$. Applying the SUSY squark searches with a heavy gluino [50], the constraint on the ψ_1 mass is $m_{\psi_2} \geq m_{\psi_1} \gtrsim 850$ GeV for $M_X \lesssim 100$ GeV and $m_{\psi_1} \gtrsim 500$ GeV for M_X close to 290 GeV. In the right panel of Fig. 3, we show the reinterpreted constraints on the effective cutoff for $y_1 y_2 = 1$.

3.3 Pair-produced Dijet Resonances plus E_T^{miss}

In this section, we perform a detailed collider study for the process of $pp \rightarrow \psi_2 \bar{\psi}_2 \rightarrow X + \psi_1 + X^\dagger + \bar{\psi}_1 \rightarrow XX^\dagger + 4j$. The collider signature is pair-produced dijet resonances plus missing transverse energy. In the left panel of Fig. 4, we show the Feynman diagram for this process. The QCD production cross

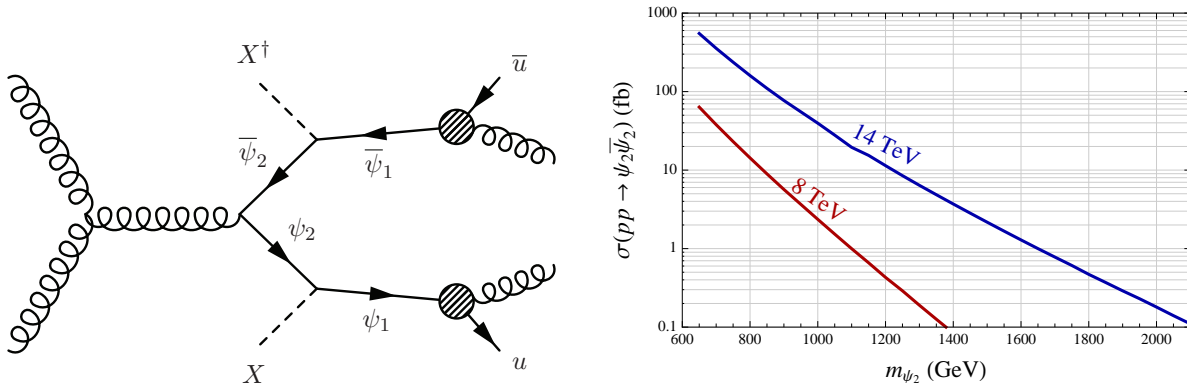


Figure 4: **Left panel:** the representative Feynman diagram for the process of $pp \rightarrow \psi_2 \bar{\psi}_2 \rightarrow X + \psi_1 + X^\dagger + \bar{\psi}_1 \rightarrow XX^\dagger + 4j$. **Right panel:** the tree-level production cross sections of $pp \rightarrow \psi_2 \bar{\psi}_2$.

sections for $\psi_2 \bar{\psi}_2$ at the LHC are the same as vector-like $t'\bar{t}'$ [53]. We show the tree-level production cross sections, calculated using `MadGraph` [39], in the right panel of Fig. 4. In the following analysis, we will ignore the signal K -factor because we will use tree-level cross sections for backgrounds.³

The main SM background comes from $Z/W^\pm + n$ jets with $Z \rightarrow \nu\bar{\nu}$ and leptonic decays of W^\pm . After comparing the results from matching parton showers and matrix elements [54], we have found that the background of parton-level $Z/W^\pm + 4$ jets with $p_T(j) > 120$ GeV provides a good estimation of total $Z/W^\pm + n$ jets background for the 8 TeV LHC. Therefore, we use $Z/W^\pm + 4$ jets as an approximation to save simulation time. There also exist additional, sub-dominant semi-leptonic $t\bar{t}$ backgrounds, which will be kept in our analysis.

Starting from the 8 TeV LHC with 19.5 fb^{-1} , we choose the model point $(m_{\psi_1}, m_{\psi_2}) = (600, 900)$ GeV as a benchmark to optimize our cuts on kinematic variables. We choose the basic cuts on the jet and missing transverse momenta to be $p_T(j_i) > 140$ GeV and $E_T^{\text{miss}} > 275$ GeV and required at least four jets satisfying the jet p_T cut in the final state. To reduce the $t\bar{t}$ and $W^\pm + \text{jets}$ backgrounds, we also veto events containing a lepton with $p_T(\ell) > 20$ GeV. Since our signal has a pair of dijet resonances with the same mass, we choose the combination among three possible dijet pairs with the smallest

³One might expect the overall significance in the later analysis to be increased by a factor of $\sim 1.2 - 1.3$ due to the inclusion of NLO effects.

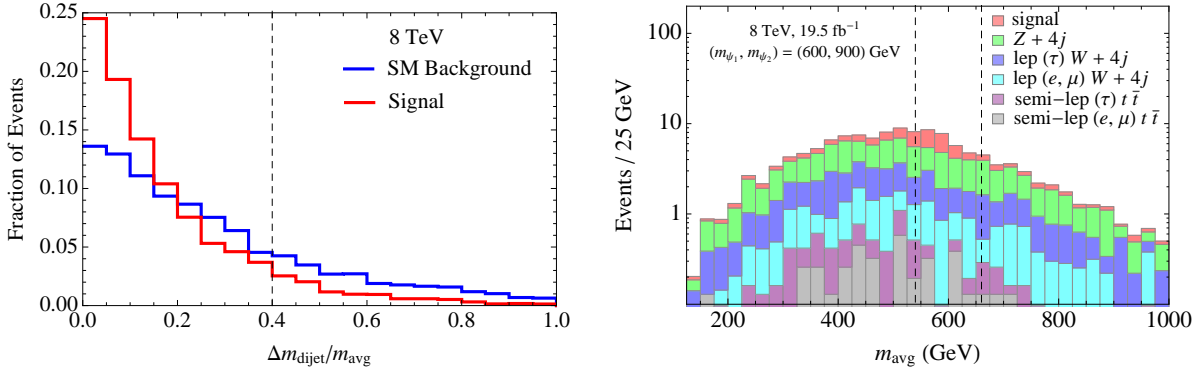


Figure 5: **Left panel:** the distributions of the fraction of events as a function of $\Delta m_{\text{dijet}}/m_{\text{avg}}$ for the signal of $(m_{\psi_1}, m_{\psi_2}) = (600, 900)$ GeV and the summed background. **Right panel:** the averaged dijet invariant mass distributions for the signal and various backgrounds, after the cut of $\Delta m_{\text{dijet}}/m_{\text{avg}} < 0.4$.

dijet invariant mass difference, Δm_{dijet} . To further reduce the SM background, we show the event fraction histogram distribution in terms of the variable $\Delta m_{\text{dijet}}/m_{\text{avg}}$ in the left panel of Fig. 5. Signal events prefer a smaller value of dijet invariant mass difference than background events. As a result, we impose a cut on this variable with $\Delta m_{\text{dijet}}/m_{\text{avg}} < 0.4$ to further increase the discovery sensitivity. In the right panel of Fig. 5, we show the averaged dijet invariant mass distribution for the signal and backgrounds. Since the signal events mainly distribute around the ψ_1 particle mass, we also impose one additional cut with $|m_{\text{avg}} - m_{\psi_1}| < 0.1 m_{\psi_1}$ to further improve the sensitivity. With the above cuts, we show the values of S/\sqrt{B} for different mass points in the left panel of Fig. 6. At 90% C.L., our simulated results show that the model point of $(m_{\psi_1}, m_{\psi_2}) = (650, 950)$ GeV can be covered, which corresponds to $\Lambda_2 \gtrsim 1.1$ TeV. Once again we see a dramatic improvement relative to the standard mono-jet signature.

At the 14 TeV LHC with 100 fb^{-1} , we choose two benchmark points with $M_X = 10$ GeV and $(m_{\psi_1}, m_{\psi_2}) = (900, 1800)$ [(900, 1500)] GeV. To optimize the discovery sensitivity, we choose the following set of cuts: at least four jets with $p_T(j) > 200$ GeV; $E_T^{\text{miss}} > 900$ [600] GeV; $\Delta m_{\text{dijet}}/m_{\text{avg}} < 0.4$ [0.3]; $|m_{\text{avg}} - m_{\psi_1}| < 0.1 m_{\psi_1}$. The signal significances, S/\sqrt{B} , for different model points are shown in the right panel of Fig. 6, taking the larger S/\sqrt{B} value from between the two benchmark points. We show the combined 90% C.L. exclusion contour in the red dashed line, which has the lower right region covered by the set of cuts for (900, 1800) GeV and the upper right region by (900, 1500) GeV. At 90% C.L., one can see that the model point of $(m_{\psi_1}, m_{\psi_2}) = (950, 1800)$ GeV can be excluded, which corresponds to $\Lambda_2 \gtrsim 1.8$ TeV.

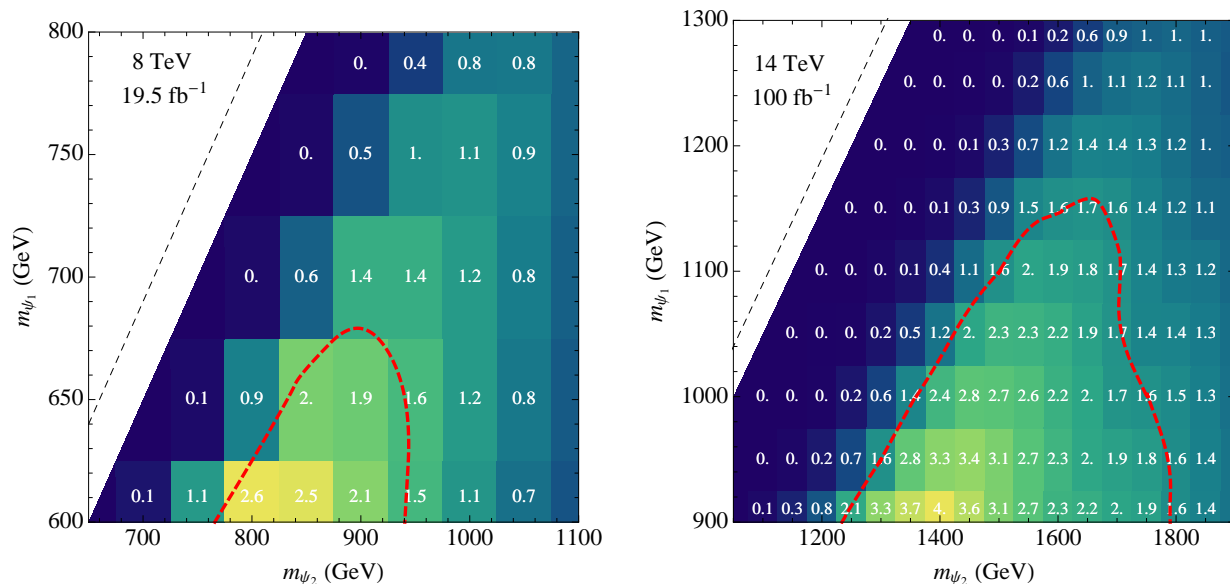


Figure 6: **Left panel:** the signal significance S/\sqrt{B} for different model points with the cuts optimized for $(m_{\psi_1}, m_{\psi_2}) = (600, 900)$ GeV and $M_X = 10$ GeV at the 8 TeV LHC with 19.5 fb^{-1} . The red dashed line is the extrapolated 90% C.L. exclusion curve. The black dashed line has $m_{\psi_2} = m_{\psi_1} + M_X$. **Right panel:** the same as the left panel but for 14 TeV with 100 fb^{-1} and the set of cuts for the combined benchmark points $(m_{\psi_1}, m_{\psi_2}) = (900, 1800)$ GeV and $(900, 1500)$ GeV with $M_X = 10$ GeV.

4 Comparison to the Direct Detection Limits

To compare with the constraints from direct detection experiments, we show the interpreted dark matter-nucleon scattering cross sections from the LHC mono-jet, $4j + E_T^{\text{miss}}$ and paired dijet+ E_T^{miss} searches in Fig. 7. In the left panel, we show the spin-independent scattering cross section including the constraints from the LUX collaboration [36]. Compared to the direct detection limits, the constraints from the LHC are not strong for heavier dark matter masses, but are more stringent for a light dark matter mass below around 5 GeV. Compared to the limits from mono-jet searches, the $4j + E_T^{\text{miss}}$ signature is definitely a more sensitive channel for constraining the spin-independent scattering cross section from the first chromo-Rayleigh interaction, $X^\dagger X G_{\mu\nu}^a G^{a\mu\nu}$.

In the right panel of Fig. 7, we show the interpreted collider constrains for the second operator, $i(XX - X^\dagger X^\dagger)G_{\mu\nu}^a \tilde{G}^{a\mu\nu}$. Here, we only show the dark matter-proton scattering cross section, since it has a larger value than dark matter-neutron one for the same dark matter mass. For the interpreted limits from collider searches and because of the additional momentum suppression with $q \approx \mu_{XA}v$, we fix the dark matter velocity to be $v = 10^{-3}$ and choose a typical target nucleus mass $m_A = 100$ GeV

in Eq. (11). Compared to the constraints from direct detection experiments, the collider searches obviously provide a more sensitive probe of this type of dark matter chromo-Rayleigh interactions.

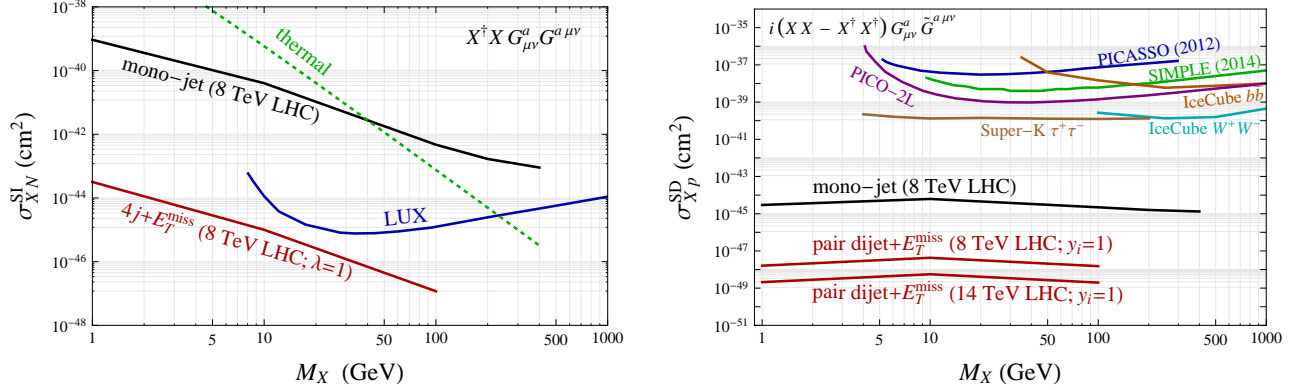


Figure 7: **Left panel:** the constraints on the dark matter spin-independent scattering cross sections from the LHC mono-jet [36] and multi-jet+ E_T^{miss} [50] searches at the 8 TeV LHC with $\sim 20 \text{ fb}^{-1}$ and the LUX direct detection experiment [55]. **Right panel:** the same as the left one but for spin-dependent dark matter-proton scattering cross sections from the LHC, SIMPLE [56], PICASSO [57], PICO-2L [58], IceCube [59] and Super-K [60]. The scattering cross section is suppressed by both the spin-dependent scattering and the exchanging momenta.

5 Discussion and Conclusions

One advantage of introducing simplified models is that the relevant model is complete from the renormalizability point of view. There is no worry about trusting theoretical descriptions of the collider limits like in the effective operator approach. On the other hand, the simplified models typically contain more model parameters and make the comparison with the results from dark matter direct or indirect detection less model-independent. For the simplified models studied here, the collider signatures highly depend on how the QCD charged particles decay. For the first operator, the color-octet scalar can decay into two gluons or two quarks plus the dark matter particle. For the second operator, the two color-triplet fermions could have many other possible decay channels beyond the ones in our paper. For instance, one could replace the operator in Eq. (26) by $\bar{\psi}_i L \sigma^{\mu\nu} u_R \tilde{B}^{\mu\nu}$, which can lead to the decay of $\psi \rightarrow u + \gamma/Z$. The final collider signature could be $2j + 2\gamma(Z) + E_T^{\text{miss}}$ with or without a pair of $j + \gamma(Z)$ resonances. To cover the majority of simplified models for dark matter chromo-Rayleigh interactions, one should search for a wide range of potential signatures.

In conclusion, we have studied simplified models to UV-complete the chromo-Rayleigh interactions

of dark matter. For the first operator, a new color-octet scalar particle could be in reach of the LHC. It may decay into just two jets or two jets plus missing transverse energy. The 8 TeV LHC can already constrain this color-octet scalar mass to be above 500-600 GeV, which can be translated into a constraint on the cutoff of the effective operator to be above 1.5-1.7 TeV. For the second operator, two QCD-charged fermions are predicted for the simplified model in this paper. A collider study of pair-produced dijet resonances plus missing energy at the 14 TeV LHC can constrain the geometric mean of the two fermion masses above around 800 GeV, which can be interpreted as a bound on the effective operator cutoff above around 1.8 TeV.

Note added: We note here that during the completion of our paper, another paper [61] appeared containing some overlap with our UV-completion of the first operator, $X^\dagger X G_{\mu\nu}^a G^{a\mu\nu}$.

Acknowledgments

We would like to thank Ran Lu for useful discussion. This work is supported by the U. S. Department of Energy under the contract DE-FG-02-95ER40896.

A Loop Level Calculations for the Coefficient of $\mathcal{O}_2^{\text{cRayleigh}}$

Starting from the Lagrangian in Eq. (23), we match the coefficient for $\mathcal{O}_2^{\text{cRayleigh}}$ at one-loop level. Other than the two Feynman diagrams in Fig. 2, we also have another four diagrams in Fig. 8 and Fig. 9.

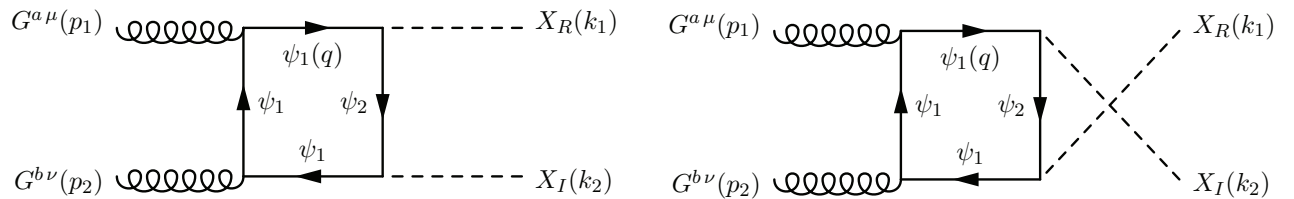


Figure 8: Loop diagrams for generating $\mathcal{O}_2^{\text{cRayleigh}}$ via a colored particle in loop..

Summing the two diagrams in Fig. 2, we have the matrix element as

$$i\mathcal{M}_1 = 4ig_s^2 y_1 y_2 \text{Tr}[t^a t^b] \varepsilon_\mu(p_1) \varepsilon_\nu(p_2) \times \int \frac{d^4 q}{(2\pi)^4} \frac{\text{Tr}[(\not{q} + m_2) \gamma^\mu (\not{q} - \not{p}_1 + m_2) \gamma^\nu (\not{q} - \not{k}_1 - \not{k}_2 + m_2) \gamma^5 (\not{q} - \not{k}_1 + m_1)]}{[q^2 - m_2^2][(q - p_1)^2 - m_2^2][(q - k_1 - k_2)^2 - m_2^2][(q - k_1)^2 - m_1^2]}. \quad (27)$$

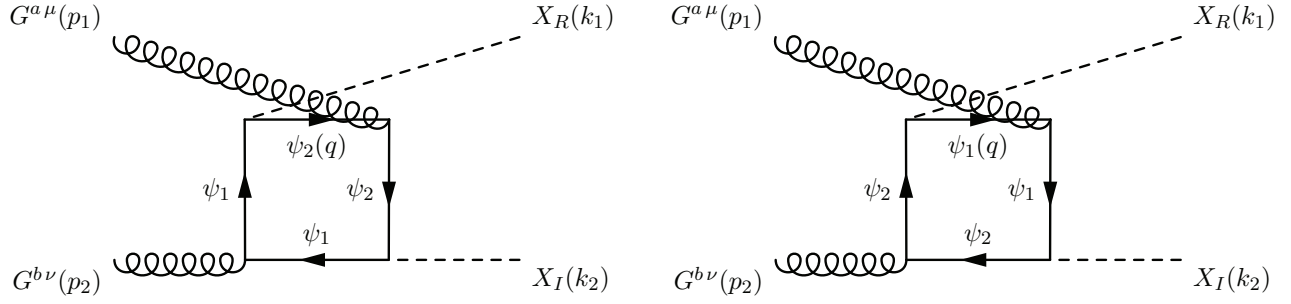


Figure 9: Loop diagrams for generating $\mathcal{O}_2^{\text{cRayleigh}}$ via a colored particle in loop..

In the heavy fermion limit, we have a simplified version of the matrix element as

$$i\mathcal{M}_1 = i \frac{g_s^2 y_1 y_2}{4\pi^2} \delta^{ab} \varepsilon_\mu(p_1) \varepsilon_\nu(p_2) \epsilon^{\mu\nu\rho\sigma} p_{1\rho} p_{2\sigma} \left[\frac{-m_1^5 + 2m_1^3 m_2^2 \log(m_1^2/m_2^2) + m_1 m_2^4}{m_2(m_1^2 - m_2^2)^3} \right]. \quad (28)$$

The two diagrams in Fig. 8 have a similar answer as $i\mathcal{M}_2 = i\mathcal{M}_1(m_1 \leftrightarrow m_2)$. The two diagrams in Fig. 9 has a summed matrix as

$$i\mathcal{M}_3 = i \frac{g_s^2 y_1 y_2}{2\pi^2} \delta^{ab} \varepsilon_\mu(p_1) \varepsilon_\nu(p_2) \epsilon^{\mu\nu\rho\sigma} p_{1\rho} p_{2\sigma} \left\{ \frac{m_1 m_2 [2(m_1^2 - m_2^2) - (m_1^2 + m_2^2) \log(m_1^2/m_2^2)]}{(m_1^2 - m_2^2)^3} \right\}. \quad (29)$$

Add all diagrams together, we have the summed matrix element

$$i\mathcal{M}_1 + i\mathcal{M}_2 + i\mathcal{M}_3 = \frac{g_s^2 y_1 y_2}{4\pi^2 m_1 m_2} \delta^{ab} \varepsilon_\mu(p_1) \varepsilon_\nu(p_2) \epsilon^{\mu\nu\rho\sigma} p_{1\rho} p_{2\sigma}. \quad (30)$$

To match to the coefficient of $\mathcal{O}_2^{\text{cRayleigh}}$, one has

$$\frac{\alpha_s y_1 y_2}{\pi m_1 m_2} = \frac{2 \alpha_s}{\pi \Lambda_2^2}. \quad (31)$$

References

- [1] M. Cahill-Rowley, R. Cotta, A. Drlica-Wagner, S. Funk, J. Hewett, et al., *Complementarity of dark matter searches in the phenomenological MSSM*, *Phys.Rev.* **D91** (2015), no. 5 055011, [arXiv:1405.6716].
- [2] A. L. Erickcek, P. J. Steinhardt, D. McCammon, and P. C. McGuire, *Constraints on the Interactions between Dark Matter and Baryons from the X-ray Quantum Calorimetry Experiment*, *Phys.Rev.* **D76** (2007) 042007, [arXiv:0704.0794].

- [3] B. A. Dobrescu, D. Hooper, K. Kong, and R. Mahbubani, *Spinless photon dark matter from two universal extra dimensions*, *JCAP* **0710** (2007) 012, [[arXiv:0706.3409](#)].
- [4] J. Bagnasco, M. Dine, and S. D. Thomas, *Detecting technibaryon dark matter*, *Phys.Lett.* **B320** (1994) 99–104, [[hep-ph/9310290](#)].
- [5] M. T. Frandsen, U. Haisch, F. Kahlhoefer, P. Mertsch, and K. Schmidt-Hoberg, *Loop-induced dark matter direct detection signals from gamma-ray lines*, *JCAP* **1210** (2012) 033, [[arXiv:1207.3971](#)].
- [6] J. Liu, B. Shuve, N. Weiner, and I. Yavin, *Looking for new charged states at the LHC: Signatures of Magnetic and Rayleigh Dark Matter*, *JHEP* **1307** (2013) 144, [[arXiv:1303.4404](#)].
- [7] S. Chang, R. Edezhath, J. Hutchinson, and M. Luty, *Effective WIMPs*, *Phys.Rev.* **D89** (2014), no. 1 015011, [[arXiv:1307.8120](#)].
- [8] H. An, L.-T. Wang, and H. Zhang, *Dark matter with t-channel mediator: a simple step beyond contact interaction*, *Phys.Rev.* **D89** (2014), no. 11 115014, [[arXiv:1308.0592](#)].
- [9] Y. Bai and J. Berger, *Fermion Portal Dark Matter*, *JHEP* **1311** (2013) 171, [[arXiv:1308.0612](#)].
- [10] A. DiFranzo, K. I. Nagao, A. Rajaraman, and T. M. Tait, *Simplified Models for Dark Matter Interacting with Quarks*, *JHEP* **1311** (2013) 014, [[arXiv:1308.2679](#)].
- [11] O. Buchmueller, M. J. Dolan, and C. McCabe, *Beyond Effective Field Theory for Dark Matter Searches at the LHC*, *JHEP* **1401** (2014) 025, [[arXiv:1308.6799](#)].
- [12] B. Batell, T. Lin, and L.-T. Wang, *Flavored Dark Matter and R-Parity Violation*, *JHEP* **1401** (2014) 075, [[arXiv:1309.4462](#)].
- [13] M. Papucci, A. Vichi, and K. M. Zurek, *Monojet versus the rest of the world I: t-channel models*, *JHEP* **1411** (2014) 024, [[arXiv:1402.2285](#)].
- [14] Y. Bai and J. Berger, *Lepton Portal Dark Matter*, *JHEP* **1408** (2014) 153, [[arXiv:1402.6696](#)].
- [15] S. Chang, R. Edezhath, J. Hutchinson, and M. Luty, *Leptophilic Effective WIMPs*, *Phys.Rev.* **D90** (2014), no. 1 015011, [[arXiv:1402.7358](#)].
- [16] P. Agrawal, Z. Chacko, and C. B. Verhaaren, *Leptophilic Dark Matter and the Anomalous Magnetic Moment of the Muon*, *JHEP* **1408** (2014) 147, [[arXiv:1402.7369](#)].

- [17] M. Garny, A. Ibarra, S. Rydbeck, and S. Vogl, *Majorana Dark Matter with a Coloured Mediator: Collider vs Direct and Indirect Searches*, *JHEP* **1406** (2014) 169, [[arXiv:1403.4634](#)].
- [18] J.-H. Yu, *Vector Fermion-Portal Dark Matter: Direct Detection and Galactic Center Gamma-Ray Excess*, *Phys.Rev.* **D90** (2014), no. 9 095010, [[arXiv:1409.3227](#)].
- [19] M. R. Buckley, D. Feld, and D. Goncalves, *Scalar Simplified Models for Dark Matter*, *Phys.Rev.* **D91** (2015), no. 1 015017, [[arXiv:1410.6497](#)].
- [20] A. Berlin, S. Gori, T. Lin, and L.-T. Wang, *Pseudoscalar Portal Dark Matter*, [arXiv:1502.06000](#).
- [21] T. Jacques and K. Nordström, *Mapping monojet constraints onto Simplified Dark Matter Models*, [arXiv:1502.05721](#).
- [22] M. Garny, A. Ibarra, and S. Vogl, *Signatures of Majorana dark matter with t-channel mediators*, [arXiv:1503.01500](#).
- [23] M. Chala, F. Kahlhoefer, M. McCullough, G. Nardini, and K. Schmidt-Hoberg, *Constraining Dark Sectors with Monojets and Dijets*, [arXiv:1503.05916](#).
- [24] N. F. Bell, Y. Cai, J. B. Dent, R. K. Leane, and T. J. Weiler, *Dark matter at the LHC: EFTs and gauge invariance*, [arXiv:1503.07874](#).
- [25] M. A. Shifman, A. Vainshtein, and V. I. Zakharov, *Remarks on Higgs Boson Interactions with Nucleons*, *Phys.Lett.* **B78** (1978) 443.
- [26] G. Belanger, F. Boudjema, A. Pukhov, and A. Semenov, *Dark matter direct detection rate in a generic model with micrOMEGAs 2.2*, *Comput.Phys.Commun.* **180** (2009) 747–767, [[arXiv:0803.2360](#)].
- [27] P. Junnarkar and A. Walker-Loud, *Scalar strange content of the nucleon from lattice QCD*, *Phys.Rev.* **D87** (2013), no. 11 114510, [[arXiv:1301.1114](#)].
- [28] H.-Y. Cheng and C.-W. Chiang, *Revisiting Scalar and Pseudoscalar Couplings with Nucleons*, *JHEP* **1207** (2012) 009, [[arXiv:1202.1292](#)].
- [29] R. J. Hill and M. P. Solon, *Standard Model anatomy of WIMP dark matter direct detection I: weak-scale matching*, *Phys.Rev.* **D91** (2015) 043504, [[arXiv:1401.3339](#)].

- [30] R. J. Hill and M. P. Solon, *Standard Model anatomy of WIMP dark matter direct detection II: QCD analysis and hadronic matrix elements*, *Phys.Rev.* **D91** (2015) 043505, [[arXiv:1409.8290](#)].
- [31] D. Diakonov, M. V. Polyakov, and C. Weiss, *Hadronic matrix elements of gluon operators in the instanton vacuum*, *Nucl.Phys.* **B461** (1996) 539–580, [[hep-ph/9510232](#)].
- [32] M. Felizardo, T. Girard, T. Morlat, A. Fernandes, A. Ramos, et al., *Final Analysis and Results of the Phase II SIMPLE Dark Matter Search*, *Phys.Rev.Lett.* **108** (2012) 201302, [[arXiv:1106.3014](#)].
- [33] **COUPP** Collaboration, E. Behnke et al., *First Dark Matter Search Results from a 4-kg CF₃I Bubble Chamber Operated in a Deep Underground Site*, *Phys.Rev.* **D86** (2012) 052001, [[arXiv:1204.3094](#)].
- [34] J. Goodman, M. Ibe, A. Rajaraman, W. Shepherd, T. M. Tait, et al., *Constraints on Dark Matter from Colliders*, *Phys.Rev.* **D82** (2010) 116010, [[arXiv:1008.1783](#)].
- [35] Y. Bai, P. J. Fox, and R. Harnik, *The Tevatron at the Frontier of Dark Matter Direct Detection*, *JHEP* **1012** (2010) 048, [[arXiv:1005.3797](#)].
- [36] **CMS** Collaboration, V. Khachatryan et al., *Search for dark matter, extra dimensions, and unparticles in monojet events in proton-proton collisions at $\sqrt{s} = 8$ TeV*, [arXiv:1408.3583](#).
- [37] **ATLAS** Collaboration, *Search for New Phenomena in Monojet plus Missing Transverse Momentum Final States using 10fb-1 of pp Collisions at $\sqrt{s}=8$ TeV with the ATLAS detector at the LHC*, ATLAS-CONF-2012-147, ATLAS-COM-CONF-2012-190.
- [38] A. Alloul, N. D. Christensen, C. Degrande, C. Duhr, and B. Fuks, *FeynRules 2.0 - A complete toolbox for tree-level phenomenology*, *Comput.Phys.Commun.* **185** (2014) 2250–2300, [[arXiv:1310.1921](#)].
- [39] J. Alwall, M. Herquet, F. Maltoni, O. Mattelaer, and T. Stelzer, *MadGraph 5 : Going Beyond*, *JHEP* **1106** (2011) 128, [[arXiv:1106.0522](#)].
- [40] T. Sjostrand, S. Mrenna, and P. Z. Skands, *A Brief Introduction to PYTHIA 8.1*, *Comput.Phys.Commun.* **178** (2008) 852–867, [[arXiv:0710.3820](#)].
- [41] J. S. Conway, *Pretty Good Simulation of high-energy collisions*, 090401 **release**.

- [42] Y. Bai, V. Barger, L. L. Everett, and G. Shaughnessy, *Two-Higgs-doublet-portal dark-matter model: LHC data and Fermi-LAT 135 GeV line*, *Phys.Rev.* **D88** (2013), no. 1 015008, [[arXiv:1212.5604](#)].
- [43] U. Haisch and E. Re, *Simplified dark matter top-quark interactions at the LHC*, [arXiv:1503.00691](#).
- [44] **CMS** Collaboration, S. Chatrchyan et al., *Search for invisible decays of Higgs bosons in the vector boson fusion and associated ZH production modes*, *Eur.Phys.J.* **C74** (2014) 2980, [[arXiv:1404.1344](#)].
- [45] Y. Bai and B. A. Dobrescu, *Heavy octets and Tevatron signals with three or four b jets*, *JHEP* **1107** (2011) 100, [[arXiv:1012.5814](#)].
- [46] R. S. Chivukula, A. Farzinnia, J. Ren, and E. H. Simmons, *Constraints on the Scalar Sector of the Renormalizable Coloron Model*, *Phys.Rev.* **D88** (2013), no. 7 075020, [[arXiv:1307.1064](#)].
- [47] M. I. Gresham and M. B. Wise, *Color octet scalar production at the LHC*, *Phys.Rev.* **D76** (2007) 075003, [[arXiv:0706.0909](#)].
- [48] Y. Bai, A. Katz, and B. Tweedie, *Pulling Out All the Stops: Searching for RPV SUSY with Stop-Jets*, *JHEP* **1401** (2014) 040, [[arXiv:1309.6631](#)].
- [49] **CMS** Collaboration, V. Khachatryan et al., *Search for pair-produced resonances decaying to jet pairs in proton-proton collisions at $\sqrt{s} = 8$ TeV*, [arXiv:1412.7706](#).
- [50] **CMS** Collaboration, S. Chatrchyan et al., *Search for new physics in the multijet and missing transverse momentum final state in proton-proton collisions at $\sqrt{s} = 8$ TeV*, *JHEP* **1406** (2014) 055, [[arXiv:1402.4770](#)].
- [51] D. Goncalves-Netto, D. Lopez-Val, K. Mawatari, T. Plehn, and I. Wigmore, *Sgluon Pair Production to Next-to-Leading Order*, *Phys.Rev.* **D85** (2012) 114024, [[arXiv:1203.6358](#)].
- [52] S. Weinberg, *Larger Higgs Exchange Terms in the Neutron Electric Dipole Moment*, *Phys.Rev.Lett.* **63** (1989) 2333.
- [53] **CMS** Collaboration, S. Chatrchyan et al., *Inclusive search for a vector-like T quark with charge $\frac{2}{3}$ in pp collisions at $\sqrt{s} = 8$ TeV*, *Phys.Lett.* **B729** (2014) 149–171, [[arXiv:1311.7667](#)].

- [54] S. Hoeche, F. Krauss, N. Lavesson, L. Lonnblad, M. Mangano, et al., *Matching parton showers and matrix elements*, [hep-ph/0602031](#).
- [55] **LUX** Collaboration, D. Akerib et al., *First results from the LUX dark matter experiment at the Sanford Underground Research Facility*, *Phys.Rev.Lett.* **112** (2014) 091303, [[arXiv:1310.8214](#)].
- [56] **SIMPLE** Collaboration, M. Felizardo et al., *The SIMPLE Phase II Dark Matter Search*, *Phys.Rev.* **D89** (2014), no. 7 072013, [[arXiv:1404.4309](#)].
- [57] **PICASSO** Collaboration, S. Archambault et al., *Constraints on Low-Mass WIMP Interactions on ^{19}F from PICASSO*, *Phys.Lett.* **B711** (2012) 153–161, [[arXiv:1202.1240](#)].
- [58] **SNO** Collaboration, C. Amole et al., *Dark Matter Search Results from the PICO-2L C_3F_8 Bubble Chamber*, [arXiv:1503.00008](#).
- [59] **IceCube** Collaboration, M. Aartsen et al., *Search for dark matter annihilations in the Sun with the 79-string IceCube detector*, *Phys.Rev.Lett.* **110** (2013), no. 13 131302, [[arXiv:1212.4097](#)].
- [60] **Super-Kamiokande** Collaboration, K. Choi et al., *Search for neutrinos from annihilation of captured low-mass dark matter particles in the Sun by Super-Kamiokande*, *Phys.Rev.Lett.* **114** (2015), no. 14 141301, [[arXiv:1503.04858](#)].
- [61] R. M. Godbole, G. Mendiratta, and T. M. P. Tait, *A Simplified Model for Dark Matter Interacting Primarily with Gluons*, [arXiv:1506.01408](#).